JGR Atmospheres

RESEARCH ARTICLE
10.1029/2020JD033572

Special Section:
Stratospheric aerosol during the post Pinatubo era: processes, interactions, and impact

Comparison of Coincident Optical Particle Counter and Lidar Measurements of Polar Stratospheric Clouds Above McMurdo (77.85°S, 166.67°E) From 1994 to 1999

Marcel Snels[1], Francesco Cairo[1], Luca Di Liberto[1], Andrea Scoccione[1], Marco Bracaglia[1], and Terry Deshler[2]

[1]National Research Council of Italy, Institute of Atmospheric Sciences and Climate (CNR-ISAC), Rome, Italy, [2]University of Wyoming, Laramie, WY, USA

Key Points:

- An empirical relation of surface area density and volume density as a function of the particle backscatter coefficient is derived
- Back scatter coefficients have been calculated with Mie theory from OPC size distributions
- Coincident ground-based lidar and balloon borne OPC measurements have been performed

Correspondence to:
M. Snels,
m.snels@isac.cnr.it

Citation:
Snels, M., Cairo, F., Di Liberto, L., Scoccione, A., Bracaglia, M., & Deshler, T. (2021). Comparison of coincident optical particle counter and lidar measurements of polar stratospheric clouds above McMurdo (77.85°S, 166.67°E) from 1994 to 1999. *Journal of Geophysical Research: Atmospheres*, *126*, e2020JD033572. https://doi.org/10.1029/2020JD033572

Received 24 JUL 2020
Accepted 29 JAN 2021

Abstract Macroscopic stratospheric aerosol properties such as surface area density (SAD) and volume density (VD) are required by modern chemistry climate models. These quantities are in continuous need of validation by observations. Direct observation of these parameters is not possible, but they can be derived from optical particle counters (OPCs) which provide concentration (number density) and size distributions of aerosol particles, and possibly from ground-based and satellite-borne lidar observations of particle backscatter coefficients and aerosol type. When such measurements are obtained simultaneously by OPCs and lidars, they can be used to calculate backscatter and extinction coefficients, as well as SAD and VD. Empirical relations can thus be derived between particle backscatter coefficient, extinction coefficient, and SAD and VD for a variety of aerosols (desert dust, maritime aerosols, stratospheric aerosols) and be used to approximate SAD and VD from lidar measurements. Here we apply this scheme to coincident measurements of polar stratospheric clouds above McMurdo Station, Antarctica, by ground-based lidar and balloon-borne OPCs. The relationships derived from these measurements will provide a means to obtain values of SAD and VD for supercooled ternary solutions (STS) and nitric acid trihydrate (NAT) PSCs from the backscatter coefficients measured by lidar. Coincident lidar and OPC measurements provided 15 profile comparisons. Empirical expressions of SAD and VD as a function of particle backscatter coefficient, β, were calculated from fits of the form $\log(\mathrm{SAD/VD}) = A + B\log(\beta)$ using β from the lidar and SAD/VD from the OPC. The PSCs were classified as STS and NAT mixtures, ice being absent.

1. Introduction

Polar stratospheric clouds (PSCs), which form in the polar stratosphere during winter and early spring, play an important role in the stratospheric chemistry processes which deplete stratospheric ozone in the Polar Regions (see e.g., Solomon, 1999). The PSC particles provide surfaces on which inactive forms of chlorine are converted into reactive, ozone-destroying forms. In addition, they remove nitrogen compounds that moderate the destructive impact of chlorine. Several particle types are observed in PSCs, both in liquid and solid phase, containing sulfuric acid, nitric acid, and water. All PSC particles form on the underlying sulfuric acid and water (sulfate) aerosol which blankets the stratosphere. These sulfate aerosols form from the condensation of oxidized sulfur which reaches the stratosphere from surface production of OCS and SO_2 and from volcanic outbursts and biomass burning (Kremser et al., 2016; Thomason & Peter, 2006). These stratospheric aerosols then form the condensation sites for PSCs in the polar regions.

The microphysical formation processes of PSCs depend on the availability of condensation nuclei, on the temperature and on the number density of water and nitric acid molecules in the gas phase. Detailed discussions of these processes can be found in Grooß et al. (2014), Hamill et al. (1996), Engel et al. (2013), Lowe and MacKenzie (2008), and Peter (1997).

Quite simply for fixed concentrations of water and nitric acid the particle type is a function of temperature. The first particle type which could exist in equilibrium with its environment is nitric acid trihydrate (NAT) at about 6 K above the ice frost point. Hanson and Mauersberger (1988) determined the stratospheric equilibrium temperatures for NAT, T_{NAT}, using laboratory measurements. Field measurements, however, indicated that NAT does not form readily (e.g., Dye et al., 1992), leading to investigation of NAT formation below T_{NAT}. Suggestions include NAT formation by homogeneous nucleation (Koop et al., 1995; Tabazadeh

et al., 2002), heterogeneous nucleation on ice (Luo et al., 2003) and on other preexisting condensation nuclei (Engel et al., 2013; Hoyle et al., 2013; Voigt et al., 2005), while others have investigated the nucleation rate for NAT using field measurements (Voigt et al., 2005; Ward et al., 2014). At temperatures near 3 K above the ice frost point nitric acid, water, and sulfuric acid can exist in the liquid phase as a supercooled ternary solution (STS) (Carslaw et al., 1995). Laboratory studies of STS (Anthony et al., 1997) investigated refractive indices for liquid aerosols of variable composition. At the ice frost point, ice seems to appear readily (Deshler et al., 2003). Water ice PSCs have a relative short formation time (the order of minutes), while STS and NAT need hours or days to grow (see e.g., Grooß et al., 2014; Hoyle et al., 2013) due to the much lower HNO_3 number densities with respect to the water vapor. As a consequence, ice PSCs form quickly below the ice frost point (T_{ice}) and evaporate fast above T_{ice}. While STS forms readily at about 3 K above T_{ice}, there is a nucleation barrier for NAT. Both STS and NAT will persist for days and weeks below their equilibrium temperatures, and may survive for some hours or days below the ice frost point and also above their formation temperature (Pitts et al., 2018). Since stratospheric aerosols grow by the uptake of water and nitric acid, their formation and possibly their successive removal by gravitational settling leads to a dehydration and denitrification of the stratosphere.

All Chemistry Climate Models (CCMs) must include a PSC module (e.g., Morgenstern et al., 2010, 2017; Zhu et al., 2018) to provide surface area density (SAD) and volume density (VD) of PSCs (mostly NAT and ice) to account for polar ozone loss. Instead of a detailed microphysics scheme to reproduce the formation of PSCs, these models use semi empirical algorithms based on temperature and mixing ratios of water and nitric acid to estimate SAD and VD. SAD is required because the heterogeneous reactions on PSCs producing reactive chlorine are proportional to SAD. VD is required to estimate dehydration and denitrification, due to the uptake of water vapor and nitric acid, and subsequent sedimentation of large PSC particles. Most CCMs are regularly compared to each other (e.g., Eyring et al., 2016) and to observations (e.g., Mercer et al., 2007). Differences in estimated ozone loss may lead to comparisons involving PSC observations. An estimate of SAD and VD from lidar measurements is a possible source of validation for the PSC output of CCMs. PSCs have been observed in Antarctica since the 1990s with ground-based lidars (Adriani et al., 2004; Córdoba-Jabonero et al., 2013; David et al., 2005; Di Liberto et al., 2014; Snels et al., 2019, 2020, 2021) and since 2006 with the satellite-borne CALIOP lidar (Pitts et al., 2018).

Because of the importance of obtaining aerosol extinction, and hence optical depth (Ridley et al., 2014), SAD and VD from lidar backscattering measurements, there have been various estimates of extinction, SAD, and VD from backscatter ratios (Jäger & Deshler, 2002, 2003; Jäger & Hofmann, 1991; Prata et al., 2017; Thomason et al., 2018). These studies have primarily focused on the extinction to backscatter ratio, with less emphasis on SAD and VD to backscatter ratio, and these studies have not included measurements in PSCs. Here we use coincident ground-based lidar and balloon-borne optical particle counter (OPC) measurements of PSCs at McMurdo Station, Antarctica, to derive an approximate relation between the particle backscatter coefficient and SAD and VD, for STS and NAT mixtures.

This study is organized as follows. Section 2 is dedicated to the OPC and lidar instruments and the measurement protocols. Prior to using the OPC estimates of SAD and VD for comparison with the lidar backscatter coefficient it is necessary to establish that the lidar and OPC, which drifts downwind from the lidar, are measuring quite similar PSCs during the coincident period. The most direct way to accomplish this is to calculate backscatter coefficient profiles from the OPC size distributions and compare these with the measured backscatter coefficient profiles of the lidar. In Section 3, we will show some typical coincident OPC and lidar measurements and explain how we calculated β_{OPC} from the size distributions. In Section 4, an empirical relation between the lidar backscatter coefficient and SAD and VD, calculated from the OPC size distributions is discussed.

2. Measurements

2.1. Optical Particle Counter Measurements

The OPC used for the measurements follows the principles of the instrument developed by Rosen (1964) but with a modified scattering angle and larger flow rate (167 $cm^3\ s^{-1}$) to make it applicable to PSC particle

Table 1
The Specifications of the Lidar System

Laser	Nd:YAG, Q-switched
Pulse energy at 532 nm	150 mJ
Repetition rate	10 Hz
Receiver	Newtonian
Diameter receiver	41.5 cm
Field of view	0.6 mrad
Vertical resolution 1994–1995	75 m
Vertical resolution 1996–1999	225 m

sizes (Hofmann & Deshler, 1991). The instrument uses white light to measure scattering at 40° in the forward direction from particles passing through a dark field microscope. Mie theory and a model of the OPC response function are used to determine aerosol size throughout the size range from 0.15 to 10.0 μm radius. To include in the size distributions a measure of the total aerosol population a similar OPC with a flow rate of 17 cm^3 s^{-1} coupled with a chamber to supersaturate the sample air stream with ethylene glycol vapor, a condensation nuclei (CN) counter, is used. Particles larger than 0.01 μm in the sample stream grow to optical detection thresholds and are counted (Campbell & Deshler, 2014; Rosen et al., 1978). The fundamental balloon-borne OPC measurements provide vertical profiles of size resolved aerosol concentration at 8–12 sizes, while a measurement of total concentration of aerosol > 0.01 μm is determined by a measurement with a CN counter in close proximity to the OPC measurement. From these measurements, unimodal/bimodal lognormal size distributions can be fitted to represent the measurements (Deshler et al., 2003). A number of aerosol parameters can then be calculated including SAD, VD, and aerosol extinction and backscatter coefficients for comparison with satellite sensors (Deshler et al., 2003; Hervig & Deshler, 1998, 2002; Kremser et al., 2016).

Discrepancies with satellite measurements of aerosol extinction after the decay of the Pinatubo stratospheric aerosol (e.g., Deshler et al., 2003) led Kovilakam and Deshler (2015) to an analysis of three possible systematic biases of the OPC measurements: anisokinetic sampling, particle evaporation in the inlet, and counting efficiency. The impact of these three issues on the measurements are: minimal, modest, and considerable. To account for the modest biases due to particle evaporations, Kovilakam and Deshler developed a model to account for particle evaporation which, depending on the altitude and size distribution, can lead to an underestimate of aerosol moments by 10%–15%. Using Kovilakam and Deshler's model, all OPC measurements are now corrected for particle evaporation in the inlet. The considerable overestimation of the instrument counting efficiency was discovered from laboratory counting efficiency measurements. These laboratory measurements led to a reanalysis of the calibration procedure and uncovered a calibration error which entered into the standard operating procedures during development of the 40° OPC for PSC measurements (Hofmann & Deshler, 1991).

While Kovilakam and Deshler suggested an algorithm to correct the OPC aerosol concentrations for this calibration error, this algorithm was never implemented. Instead a more fundamental approach to correct for the calibration error was developed by Deshler et al. (2019). Deshler and coworkers reanalyzed the laboratory measurements of Kovilakam and Deshler, implementing several further refinements of the measurements, and came to the conclusion that the proper way to correct for the calibration error, was not by correcting the number concentration, but by adjusting the size of each channel boundary to be at the 50% counting efficiency point which is assumed of all OPCs. Further they pointed out that OPC counting efficiencies are not simple Heaviside step functions, but more complicated cumulative distribution functions of Gaussian distributions, with the mean of the cumulative distribution function defining the channel boundary. Including this counting efficiency function into the measurement description led to a revision of the method to derive uni/bimodal lognormal size distributions from the OPC measurements. These revisions have now been applied to all the measurements and lead to a significant improvement in the agreement of OPC derived extinctions, from fitted size distributions, with satellite measured extinctions (Desh-

Table 2
A List of Coincident OPC and Lidar Data is Reported, Together With the Launch Time of the Balloon and the Start Time of the Lidar Acquisition, Both in UTC

Day	Month	Year	OPC launch time	Lidar start time	Used in analysis
23	8	1994	10:19	11:00	Yes
5	9	1994	10:34	11:30	Yes
12	9	1994	06:29	08:30	Yes
16	9	1994	13:55	14:30	Yes
22	8	1995	1:00	2:00	No
26	8	1995	5:00	6:50	No
29	8	1995	14:24	14:35	Yes
2	9	1995	10:34	10:00	Yes
23	8	1996	10:05	09:40	Yes
22	8	1997	07:41	08:40	Yes
15	9	1998	02:53	02:20	Yes
14	7	1999	22:48	23:00	Yes
2	8	1999	22:45	22:57	No
21	8	1999	03:22	05:15	Yes
28	8	1999	02:38	02:40	Yes
30	8	1999	01:12	02:00	Yes
7	9	1999	20:24	21:10	Yes
16	9	1999	01:55	01:25	Yes

Note. The last column indicates which data have been used in our analysis.
Abbreviation: OPC, optical particle counter.

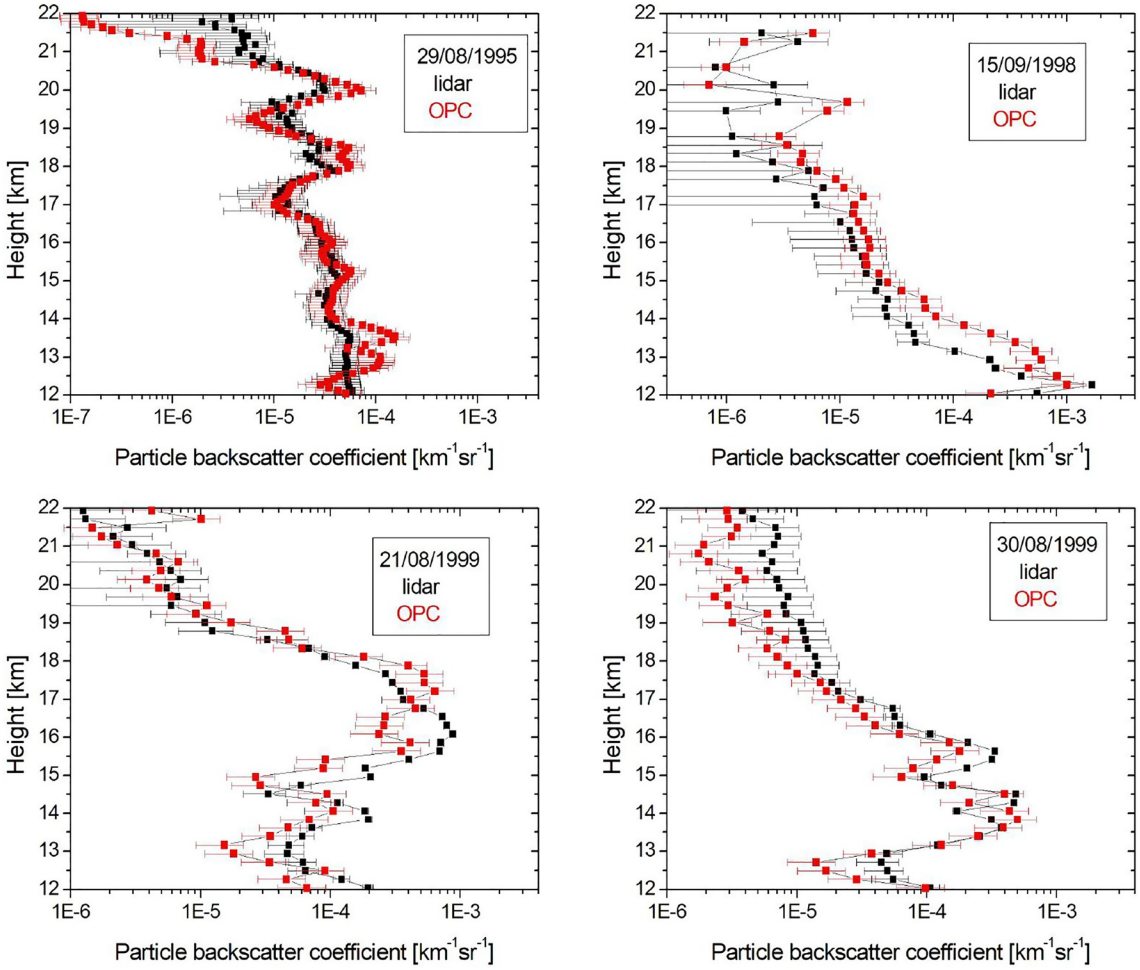

Figure 1. Particle backscatter coefficient as observed by the lidar versus the calculated value obtained from four coincident OPC measurements. The dates are indicated in the figure. OPC, optical particle counter.

ler et al., 2019). The corrections of the OPC measurements for particle evaporation and counting efficiency have been applied to all the OPC measurements presented here.

OPC measurements do not allow a straightforward classification of PSC particles. However, an approximate classification can be made, based on the local temperature and the size of the particles. At temperatures above T_{NAT}, only sulfate aerosols are possible. NAT may or may not be present at $T < T_{NAT}$ while STS will only appear near $T < T_{NAT}$–3 K. Due to the absence of a nucleation barrier, STS particle growth tends to be limited so that STS particles have greater number density and smaller particle dimensions than NAT particles which are expected to be of smaller number density, but with a radius generally larger than 0.5 μm. Due to the greater availability of water vapor, ice particles can grow larger, often with linear dimensions larger than 4–5 μm.

2.2. McMurdo Lidar Observations of PSCs

The lidar observations reported here have been recorded with a lidar system employed from 1990 to 2003 at McMurdo which consisted of a laser emitting at 532 nm and a Newton telescope with two detection channels for lidar signals with parallel and perpendicular polarization with respect to the linear polarization of the laser (Adriani et al., 2004). The main characteristics of this lidar are displayed in Table 1 (see also Adriani et al., 1992). In 2004, this lidar was replaced with a lidar system with superior characteristics which was operational until 2010 (Di Liberto et al., 2014) at McMurdo and was then moved to Dome C where it

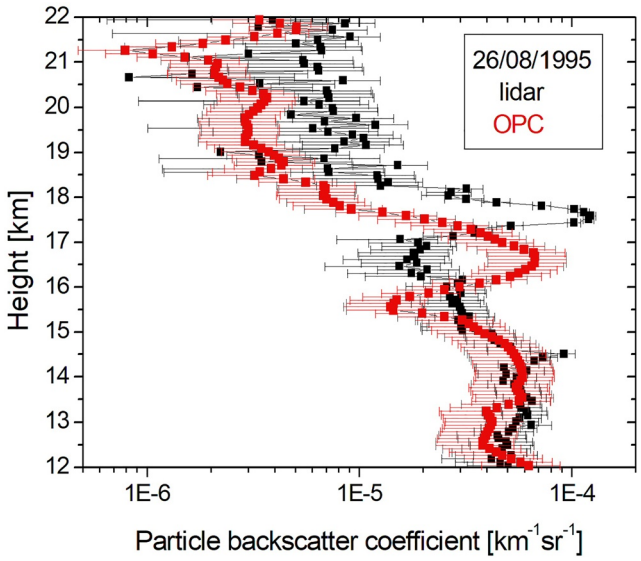

Figure 2. Particle backscatter coefficient as observed by the lidar versus the calculated value obtained from a coincident OPC measurement on the 26th August of 1995. OPC, optical particle counter.

has been active since 2014 (Snels et al., 2020, 2021). The lidar used from 1990 to 2003 allowed the measurement of backscatter ratio, volume depolarization and aerosol depolarization from 10 to 23 km. The backscatter ratio is defined as

$$R = \frac{\beta_{particles} + \beta_{molecules}}{\beta_{molecules}} \quad (1)$$

and the volume polarization as

$$\delta^{vol} = \frac{\beta_{\perp}}{\beta_{\parallel}} \quad (2)$$

The aerosol polarization can be expressed as

$$\delta^{aerosol} = \frac{\beta_{\perp}^{aerosol}}{\beta_{\parallel}^{aerosol}} = \frac{(1+\delta^{mol})\delta^{vol}R - (1+\delta^{vol})\delta^{mol}}{(1+\delta^{mol})R - (1+\delta^{vol})} \quad (3)$$

where

$$\delta^{mol} = \frac{\beta_{\perp}^{mol}}{\beta_{\parallel}^{mol}} \quad (4)$$

The backscatter coefficient was retrieved using the Klett algorithm and a correction was applied to account for the attenuation by molecules and particles (the latter by using the formulas reported by Gobbi, 1995). The depolarization was calibrated following the method described in Snels et al. (2009). The lidar was operated by science technicians of the National Science Foundation (NSF) during the Antarctic winter, typically from the end of May until the end of September to cover the whole period of PSC occurrence from 1991 until 2010. Typically the measurements were integrated over 30–60 min. The vertical resolution of the raw data was 75 m in 1994 and 1995 and 225 m in the other years. For comparison with the OPC data which has been averaged to a vertical resolution of 250 m, the OPC data have been interpolated on the vertical grid of the lidar data. Potential vorticity reanalysis shows that McMurdo is well within the stratospheric polar vortex from mid-June to the end of September, except for rare events of major vortex perturbation. A classification of the observed PSCs has been made by using the optical parameters; liquid PSCs have negligible aerosol depolarization ($\delta^{aerosol} < 0.03$ and $R > 1.25$), while ice clouds have a high backscatter ratio ($R > 10$ and $\delta^{aerosol} > 0.03$). Solid NAT particles have intermediate backscatter ratio and depolarization (all measurements with $1.15 < R < 10$ and $\delta^{aerosol} > 0.03$). All observations with $R < 1.15$ or negative values for $\delta^{aerosol}$ are not considered PSCs. Experimental errors in the backscatter ratio R are estimated to be 5%, but not less than 0.05, while the error in the aerosol depolarization is about 10%–15% (Adriani et al., 2004).

3. Comparison of Coincident OPC and Lidar Measurements

The purpose of this study is to derive approximate relations between the particle backscatter coefficient observed by lidar and the SAD and VD calculated from size distributions obtained from coincident OPC measurements. An ideal coincident measurement assumes that both instruments observe the same air mass at the same time. The balloon-borne OPC is launched at a short distance from the lidar station and should keep the same distance from the column of air probed by the lidar as long as the wind velocity is negligible. In reality, the balloon carrying the OPC drifts 50–100 km downrange from the lidar and the OPC will measure PSCs that were earlier in the vicinity of the lidar with some variations introduced by wind direction and the horizontal scale of the PSCs. Table 2 summarizes the times of the lidar and OPC measurements considered for comparison including some of which were ruled out due to differences in the vertical structure of the PSCs. The duration of the lidar acquisition is usually about 30–60 min, while the ascending balloon takes about 60 min to reach 20 km of altitude, thus the PSCs, which generally occur between 15 and 22 km, are measured by the OPC between 40 and 80 min after the release of the balloon.

Table 3
The Real Part of the Refractive Index Around 532 nm for Different Aerosol Types as Reported in Literature

Class	Refractive index	Wavelength (nm)	Ref
Volcanic aerosol	1.39–1.47	532	Adriani et al. (1995)
Sulfates	1.47	550	Erlick (2006)
STS	1.36–1.42	532	Adriani et al. (1995)
STS	1.43	532	Luo et al. (1996)
STS	1.45	532	Mehrtens et al. (1999)
STS	1.43–1.49	532	Deshler et al. (2000)
STS	1.51–1.55	532	Scarchilli et al. (2005)
α-NAT	1.51	632	Middlebrook et al. (1994)
β-NAT	≥1.46	632	Middlebrook et al. (1994)
NAT	1.38–1.46	532	Adriani et al. (1995)
NAT	1.46–1.54	532	Deshler et al. (2000)
NAT	1.37–1.45	532	Scarchilli et al. (2005)
Ice	1.31–1.33	532	Adriani et al. (1995)
Ice	1.31–1.33	532	Scarchilli et al. (2005)
Ice	1.31	532	Warren and Brandt (2008)

Abbreviations: NAT, nitric acid trihydrate; STS, supercooled ternary solutions.

Considering the horizontal and temporal differences in all available coincident lidar and OPC measurements over McMurdo, we needed a method to ensure that the PSCs measured by both instruments were relatively similar. This required that we calculate particle backscatter coefficients from the OPC size distributions for comparison with the lidar profiles of backscatter. Thus we have calculated the particle backscatter coefficient profile for all the possible coincident OPC data using Mie scattering theory for spherical particles and appropriate indices of refraction for the observed PSC types.

3.1. Comparison of Some Coincident OPC and Lidar Measurements

In total, we have 18 coincident OPC lidar measurements (see Table 2), with a small time difference between the launch of the balloon-borne OPC and the start of the lidar measurement. Typically the time difference is less than 1 h.

Figure 1 shows four examples of coincident profiles used for the present analysis. In almost all profiles, the main features have been captured by the two instruments, and 70% of the observations agree within the error bars. The discrepancies that are larger than the sum of the errorbars are probably due to the fact that both instruments do not probe exactly the same air masses and because of the approximate assumptions for the calculation of the backscatter coefficient from OPC size distributions. The calculation of β_{OPC} will be explained below. After visually comparing all coincident measurements a subset of 15 profiles (see Table 2) has been used to obtain empirical relations between the lidar particle backscatter coefficient and SAD and VD from OPC data. In one profile there is an evident altitude shift between lidar and OPC data, shown in Figure 2. This profile has been excluded from our analysis, as well as two other profiles with negligible presence of PSCs. Furthermore all lidar data points, within a profile, with a signal-to-noise ratio smaller than 2 have been excluded from our analysis.

3.2. Calculation of the Backscatter Coefficient From the OPC Size Distribution

3.2.1. Choice of Refractive Indices

The refractive index for ice is well known (Warren & Brandt, 2008), and is much lower than that for the other PSC classes (STS, NAT) and volcanic aerosol. The refractive index for STS depends on the relative concentrations of H_2SO_4, H_2O, and HNO_3; Luo et al. (1996) calculated a value of 1.43 for typical stratospheric

Table 4
The Classification of the Particles Measured by the OPC

Temperature	Radius	Classification	Refractive index
$T > T_{NAT}$	All	Volcanic aerosols or sulfates	1.44
T_{NAT}–3 K < T < T_{NAT}	All	NAT	1.48
T_{ice}< T < T_{NAT}–3 K	$R < 0.5\ \mu m$	STS	1.44
T_{ice}< T < T_{NAT}–3 K	$R > 0.5\ \mu m$	NAT	1.48
$T < T_{ice}$	$R < 0.5\ \mu m$	STS	1.44
$T < T_{ice}$	0.5 μm < R < 4 μm	NAT	1.48
$T < T_{ice}$	$R > 4\ \mu m$	Ice	1.31

Abbreviations: NAT, nitric acid trihydrate; OPC, optical particle counter; STS, supercooled ternary solutions.

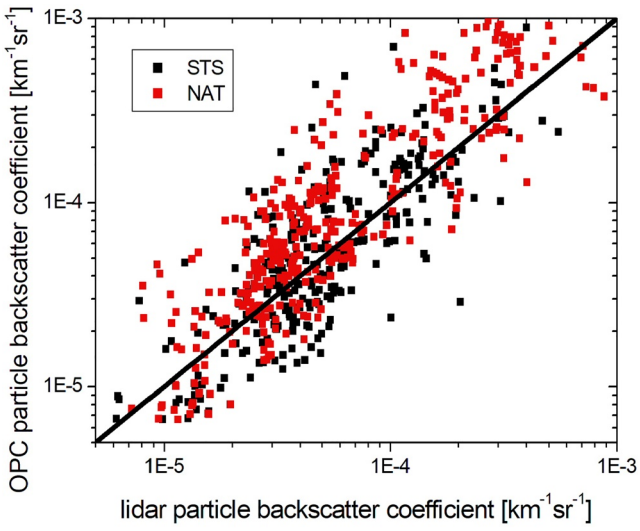

Figure 3. Calculated backscatter coefficient from the OPC size distributions without a correction for asphericity for NAT and ice versus the particle backscatter coefficient as observed by lidar. NAT, nitric acid trihydrate; STS, supercooled ternary solutions; OPC, optical particle counter.

conditions (55 mbar, 5 ppm H_2O, 10 ppb HNO_3, 0.46 ppb H_2SO_4). Laboratory measurements of the refractive index of NAT in two different crystalline forms, α and β NAT (Weiss et al., 2016) have been performed (Middlebrook et al., 1994), producing values between 1.46 (β NAT) and 1.51 (α NAT). The β form is the more stable one, and prevails at temperatures above 185 K.

Several efforts have been made to combine coincident OPC and backscatter measurements to derive a range of values for the refractive indices of different PSC classes. Adriani et al. (1995) examined lidar and OPC observations above McMurdo (78°S) in 1992, and determined refractive indices of 1.39–1.47, 1.36–1.42, 1.38–1.46, and 1.31–1.33 for volcanic aerosols, STS, NAT, and ice, respectively. Deshler et al. (2000) used a series of OPC and optical scattering measurements above Andoya (69°N) to estimate the refractive index for nondepolarizing (STS) and depolarizing particles (NAT), resulting in values of 1.43–1.49 and 1.46–1.54 for STS and NAT respectively. Scarchilli et al. (2005) used a combination of balloon-borne OPC and backscatter sonde measurements to infer the refractive index of PSCs observed on two balloon flights above Kiruna in 2000 and 2001. They used *T*-matrix calculations to calculate the backscatter coefficients from particle size distributions obtained with the OPC and tried to obtain the best match with the backscatter sonde data. They considered all particles with a radius below 0.56 μm as liquid particles and all larger particles as solid oblate or prolate spheroids. with an aspect ratio. By varying aspect ratio and refractive index, they determined a range of values that provided the best match, 1.37–1.45 for NAT particles, 1.51–1.55 for liquid particles, and 1.31–1.33 for ice. The indices of refraction reported in literature just discussed, for wavelengths around 532 nm are summarized in Table 3.

These different analyses of simultaneous observations with OPC and lidar or backscatter sonde and the different laboratory measurements do not allow for a straightforward comparison.

Here we decided to use values of 1.31, 1.44, and 1.48 for ice, STS, and NAT respectively, values that were shown to be compatible with the large PSC data set produced by the CALIPSO observations (Hoyle et al., 2013; Pitts et al., 2018), and that are intermediate between those reported for STS and NAT by Adriani et al. (1995), Deshler et al. (2000), and Scarchilli et al. (2005). For the background aerosol, that is, those present at $T > T_{NAT}$, we assume a refractive index of 1.44 (Steele & Hamill, 1981).

Generally, a size distribution of particles measured by the OPC may consist of different species, depending on the size and the temperature. Thus size and temperature have been used for dividing the size distribution in different parts assigned to the different PSC types (STS, NAT mixtures, and ice) according to the criteria displayed in Table 4. The backscatter coefficient for each size distribution has been calculated as the sum of the contributions of each species, adopting the proper refractive index for each of them.

PSC observations by the ground-based and satellite-borne lidar, CALIOP, showed that ice is observed almost exclusively below the ice frost point, while STS and NAT have been observed in a wider temperature range, from below the ice frost point to above the equilibrium temperature for STS and NAT (e.g., Pitts et al., 2018). Here we assume that all particles observed above T_{NAT} are sulfates. At temperatures between T_{NAT}–3K and T_{NAT}, only NAT can exist. For temperatures below T_{NAT}–3K, we adopt a threshold radius of 0.5 μm, similar to the one proposed in Scarchilli et al. (2005), to distinguish between NAT and STS; all particles with a radius less than 0.5 μm are STS while larger particles are NAT. Since there is no nucleation barrier for STS, it is fair to assume that all the smaller particles are primarily STS. If the temperature is below the ice frost point, we might have liquid STS, NAT, and ice particles at the same time. In this case, we assign the larger particles to ice, and the smaller to STS or NAT, by assuming a minimum threshold radius for ice (e.g., 4 μm).

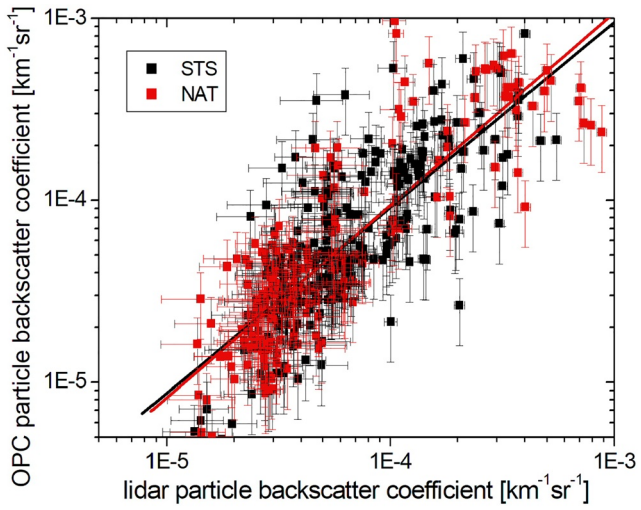

Figure 4. Calculated backscatter coefficient from the OPC size distributions with a correction of 0.5 for NAT and ice versus the particle backscatter coefficient as observed by lidar with errorbars, The black and red lines are linear fits for STS and NAT mixtures with $\log(\beta_{opc}) = -0.15 + 0.97 \log(\beta_{lidar})$ for the STS mixtures and $\log(\beta_{opc}) = -0.10 + 0.98 \log(\beta_{lidar})$ for the NAT mixtures. NAT, nitric acid trihydrate; OPC, optical particle counter; STS, supercooled ternary solutions.

In Figure 3, the backscatter coefficient calculated from the OPC size distributions is compared to the particle backscatter coefficient obtained from coincident lidar observations. We used all lidar data from 12 to 22 km. All OPC data have been obtained at a vertical grid of 250 m, while the grid of the lidar measurements varied throughout the years, from 75 to 225 m. To compare OPC and lidar data, all OPC data have been interpolated on the lidar vertical grid. In average, the calculated values for the NAT mixtures are about 60% too high, while the STS values are only slightly higher.

It is well known that the backscatter coefficient calculated for solid particles requires a correction for asphericity. An educated guess of the magnitude of such correction can be provided by looking at studies comparing the phase function and the backscatter cross section calculated with the *T*-matrix method for aspherical scatterers compared to spherical scatterers (see e.g., Mishchenko et al., 1996). The ratio of these varies from 0.65 to 0.35 for oblate and prolate spheroids with an asymmetry parameter varying from 1.4 to 2.0 (Mishchenko et al., 1996). Other studies suggest to use an ensemble of spheroids with different aspect ratios to simulate the scattering properties of aspherical particles (Dubovik et al., 2006; Liu et al., 2006; Mishchenko et al., 1997). A detailed study of the correction of the calculated backscatter coefficient for aspherical particles would require a computational effort which is beyond the scope of this work. Thus we propose a simplified correction for the aspherical particles by multiplying the calculated backscatter coefficient for NAT and ice with a factor of 0.5, of course limited to the NAT and ice particle fraction in each size distribution, to take into account their asphericity. When applying this correction for the solid particles in the calculations, by multiplying the contribution of the solid particles by a factor of 0.5, the agreement becomes much better, as can be seen in Figure 4. Note that the asphericity correction has an effect only on the calculated backscatter coefficient of the solid particles, and not on the total backscatter coefficient, which includes also liquid particles. It can be seen that the correction for asphericity has also a small impact on the STS mixtures, since the STS mixtures may contain a small subset of solid particles. This agreement can be quantified by fitting $\log(\beta_{opc}) = A + B \log(\beta_{lidar})$, resulting in $\log(\beta_{opc}) = -0.15 + 0.97 \log(\beta_{lidar})$ for the STS mixtures and $\log(\beta_{opc}) = -0.10 + 0.98 \log(\beta_{lidar})$ for the NAT mixtures. The slopes of these fits near 1.0 and the small offsets indicate that the two instruments are measuring quite similar PSCs within the coincident data set, and that the OPC does a reasonable job of simulating the lidar backscatter measurements.

Table 5
The Difference $(\beta_{var}-\beta_{calc})/\beta_{calc}$, Averaged Over all Calculated Values is Displayed in Function of Radius 1 and 2, Discriminator Between STS and NAT and NAT and Ice, Respectively, the Refractive Indices of STS and NAT, and the Correction for Aspherical Particles

Parameter	Value	Reference value	Difference (%)
Radius 1 (μm)	0.75	0.5	+3.9
Radius 1 (μm)	1.0	0.5	+7.5
Radius 2 (μm)	5	4	+0.7
Refractive index STS	1.42	1.44	−4.6
Refractive index STS	1.46	1.44	+4.8
Refractive index NAT	1.46	1.48	−1.6
Refractive index NAT	1.50	1.48	+0.7
Asph. correction	0.7	0.5	+14.7
Asph. correction	0.9	0.5	+29.4

Abbreviations: NAT, nitric acid trihydrate; STS, supercooled ternary solutions.

We can estimate the impact of our choices of refractive index, classification method, and asphericity correction on the calculated backscatter coefficients. To obtain such an estimate we vary all parameters with respect to the ones used in the calculations and compute the variation on the backscatter coefficient, averaged over all the altitudes between 12 and 22 km of all coincident profiles. The results are displayed in Table 5. The choice of the two threshold radii was found to be not very critical; while increasing the threshold radius to separate STS from NAT, from 0.5 μm to 0.75 and 1 μm, the particle backscatter coefficient, calculated as indicated below, increased by only 3.9% and 7.5% respectively. The upper threshold radius, separating NAT and ice was also varied from 4 to 5 μm, leading to an average increase of 0.7% in the calculated backscatter coefficient. While the choice of the refractive indices has a minor impact on the calculations, the correction for asphericity has a major effect. It is also evident from Table 5 that different choices of the parameters may also provide a reasonable agreement with the lidar profiles.

Table 6
The Parameters Resulting From the Fit Log(Y) = A + B Log(β_p), Where Y = (SAD, VD), Comparing Fits With Respect to the Backscatter Coefficients Obtained From the 15 Coincident Lidar Measurements and Those Calculated From the Same Coincident OPC Data

	Wrt backscatter coefficient lidar ($km^{-1}sr^{-1}$)				Wrt calculated backscatter coefficient ($km^{-1}sr^{-1}$)			
	STS mixtures		NAT mixtures		STS mixtures		NAT mixtures	
Constant	A	B	A	B	A	B	A	B
Surface area density ($\mu m^2\ cm^{-3}$)	4.17(14)	0.80(4)	4.41(16)	0.89(4)	4.30(4)	0.83(1)	4.29(4)	0.86(2)
Volume density ($\mu m^3\ cm^{-3}$)	4.24(17)	1.05(4)	3.95(18)	0.96(5)	4.24(7)	1.05(1)	3.93(6)	0.96(2)

Note. The numbers between parentheses are the statistical errors in the last digits.
Abbreviations: NAT, nitric acid trihydrate; SAD, surface area density; STS, supercooled ternary solutions; VD, volume density.

4. Empirical Relation Between the Lidar Particle Backscatter Coefficient and SAD and VD From OPC Data

Several authors tried to obtain a functional relation linking the particle backscatter coefficient β_p with SAD and VD. Gobbi (1995) calculated backscatter and extinction coefficients, as well as SAD and VD for a variety of particle densities and size distributions. He used a Monte Carlo technique to generate random bimodal lognormal distributions, whose parameters were constrained by observations of clouds in the stratosphere, mostly at mid-latitude (between 26° − 42°N). Most simulations used refractive indices from 1.43 to 1.45. However, the refractive indices of several Monte Carlo runs were set from 1.3 to 1.5 in order to include PSC particles, but without changing the boundaries of the bilognormal distributions. SAD, VD and particle extinction coefficients σ_p were then calculated for all assumed size distributions within the boundaries set for the bilognormal distributions and refractive indices and fitted to relations of the form $\log(Y) = A + B\log(\beta_p) + C\log(\beta_p)^2$, where Y = SAD, VD, or σ_p. Although PSCs are possibly included in some of the simulations, the results are not specific for PSCs.

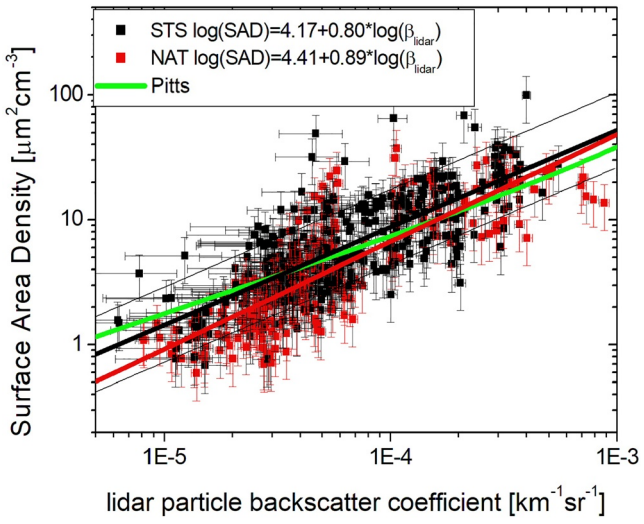

Figure 5. SAD versus particle backscatter coefficient for the coincident data, divided in STS mixtures (black squares) and NAT mixtures (red squares). The thick black and red lines are linear fits of the form $\log(VD) = A + B\log(\beta_p)$ for the STS and NAT mixtures. The thin black lines are a factor of two lower/higher than the fit for STS. The green line uses the relation between β_p and SAD derived in Pitts et al. (2018). NAT, nitric acid trihydrate; SAD, surface area density; STS, supercooled ternary solutions; VD, volume density.

Recently Pitts et al. (2018) reported calculations of SAD and VD for both liquid and solid PSCs based on a number of assumptions supported by lidar observations. For spherical liquid particles, a unimodal lognormal distribution was assumed with $\sigma = 1.6$ and a mode radius depending on the number density of the liquid particles and the equilibrium condensed liquid particle VD (Carslaw et al., 1995). SAD and VD were also calculated for NAT and ice PSCs, assuming unimodal lognormal distributions with $\sigma = 1.38$ and a range of volume-equivalent radii from 0.25 to 15 μm. The backscatter coefficients were calculated using Mie scattering theory (Mishchenko et al., 1996), with refractive indices of 1.44 and 1.48, for STS and NAT mixtures, respectively. NAT mixtures were assumed to be prolate spheroids with an aspect ratio of 0.9. More details can be found in Pitts et al. (2018). A polynomial function of the form $\log(SAD/VD) = A + B\log(\beta_p) + C\log(\beta_p)^2 + D\log(\beta_p)^3$ was fitted to a multitude of lognormal distributions for liquid PSCs.

Here we start from particle backscatter coefficients measured by the lidar, limited to those with a sufficiently high signal-to-noise ratio and disregarding obviously "bad" coincidences such as can be seen in Figure 2. We also exclude all data where the signal-to-noise ratio of the measured backscatter coefficient is less than two. The SAD and VD have been calculated from coincident OPC size distributions, interpolated on the vertical grid of the lidar data.

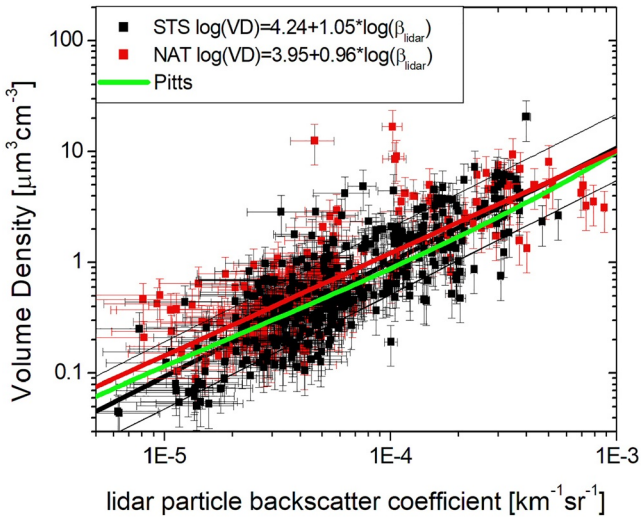

Figure 6. VD versus particle backscatter coefficient for the coincident data, divided in STS mixtures (black squares) and NAT mixtures (red squares). The thick black and red lines are linear fits of the form $\log(VD) = A + B\log(\beta_p)$ for the STS and NAT mixtures. The thin black lines are a factor of two lower/higher than the fit for STS. The green line uses the relation between β_p and VD derived in Pitts et al. (2018). NAT, nitric acid trihydrate; SAD, surface area density; STS, supercooled ternary solutions; VD, volume density.

This analysis uses the most extensive data set of coincident OPC and lidar observations in polar regions up to now, consisting of 15 coincident measurements recorded from 1994 to 1999, mostly from the 22nd of August until the 16th of September above McMurdo (see Table 2), showing mainly liquid PSCs and mixtures of solid NAT particles and STS as well as background aerosols, ice never being observed.

Since we want to compare our results with those of Pitts et al. (2018), we have performed the analysis for STS and NAT mixtures separately, using the classification obtained from the optical parameters measured by the lidar.

A fit of the coincident data for STS and the NAT mixtures to the functional relation of the form $\log(SAD/VD) = A + B\log(\beta_p)$ yields four sets of constants A and B (see Table 6 and Figures 5 and 6). Of course these values are valid only in the range of backscatter coefficients reported in Figures 5 and 6.

In Figure 5, one can observe that the SAD for STS can be reasonably well fitted to the equation $\log(SAD) = A + B\log(\beta_p)$, although with a large spread around the fit. Pitts et al. (2018) derived curves for the SAD of liquid particles and a range of values for NAT mixtures and ice, with estimated uncertainties of ±1, ±2.5 and ± 5 $\mu m^2\ cm^{-3}$, for $\beta = 10^{-5}$, 10^{-4} and $5 \times 10^{-4}\ km^{-1}sr^{-1}$, respectively. The spread of the points derived from the coincident measurements with respect to the empirical fit for liquid particles is generally larger than the uncertainties reported by Pitts et al. (2018). This is most probably due to the experimental uncertainties and to the fact that the coincidence of the air masses observed by lidar and OPC is not perfect. NAT mixtures are generally located below the STS empirical fit, in good agreement with computations by Pitts and coworkers (see Figure 8 in Pitts et al., 2018).

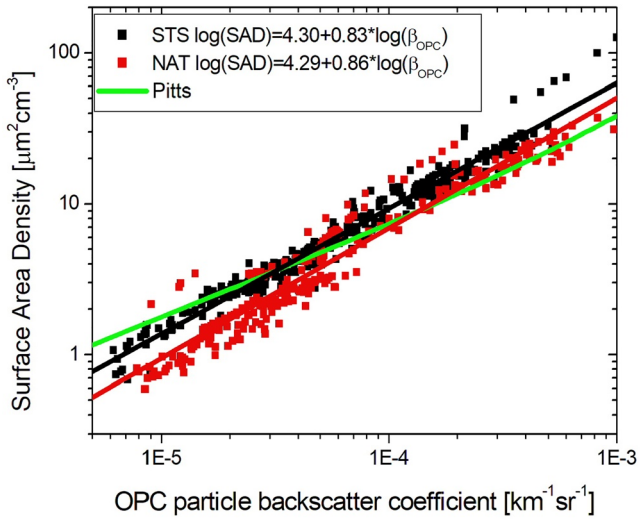

Figure 7. SAD versus particle backscatter coefficient calculated from the coincident OPC data, divided in STS mixtures (black squares) and NAT mixtures (red squares). The thick black and red lines are linear fits of the form $\log(VD) = A + B\log(\beta_p)$ for the STS and NAT mixtures. NAT, nitric acid trihydrate; OPC, optical particle counter; SAD, surface area density; STS, supercooled ternary solutions; VD, volume density.

Figure 6 shows how VD of STS is fitted by the expression $\log(VD) = A + B\log(\beta_p)$. The uncertainties in the curve derived by Pitts et al. are ±0.05, ±0.15 and ± 1 $\mu m^3\ cm^{-3}$, for $\beta = 10^{-5}$, 10^{-4}, and $5 \times 10^{-4}\ km^{-1}sr^{-1}$, respectively. Again, the spread of the experimental points around the fit to the coincident measurements is larger than the uncertainties reported for the curve from Pitts et al., probably for the same reasons as for the SAD fit, but still 70% of all STS points are within a factor of two of the fit.

According to Pitts et al. (2018), the VD of the NAT mixtures should be distributed above and below the liquid particle approximation (see Figure 9 in Pitts et al., 2018), but with a preference for higher values. Here we observe that the VD of the NAT mixtures is slightly above the fit for the STS data, which is again in good agreement with Pitts et al. (2018). Figures 5 and 6 are in agreement with the calculations made by Pitts et al. (2018), although the observed OPC size distributions are often bimodal lognormal distributions, instead of the ensemble of single-mode lognormal distributions used by Pitts et al. (2018).

A different approach would be to start from the particle backscatter coefficients calculated from the size distributions measured by the OPC, following the method explained above. If we want to distinguish between STS and NAT mixtures, we have to restrict the fits to OPC data coincident with the lidar measurements, since the classification of PSC types from OPC data alone is not contemplated here. Thus fits of calculated particle backscatter coefficients to calculated SAD and VD were

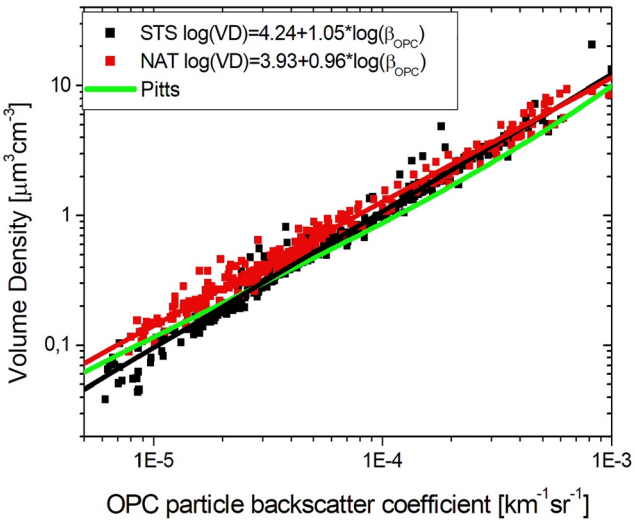

Figure 8. SAD versus particle backscatter coefficient calculated from the coincident OPC data, divided in STS mixtures (black squares) and NAT mixtures (red squares). The thick black and red lines are linear fits of the form $\log(VD) = A + B\log(\beta_p)$ for the STS and NAT mixtures. NAT, nitric acid trihydrate; OPC, optical particle counter; SAD, surface area density; STS, supercooled ternary solutions; VD, volume density.

performed using the same OPC data set as used in the coincident measurements above and show essentially the same results (see Figures 7 and 8), but with a lower scattering of the data with respect to the fitted line. The small spread of the fitted quantities from the fitted line when using the OPC particle backscatter coefficients, compared to the fits using the lidar measured backscatter, may in large part be due to the imperfect match of the PSCs captured by the coincident lidar and OPC measurements. When the OPC is used for calculating both backscatter and SAD/VD, there is no question but what the measurements are in the same PSC. The similarity of the fitting parameters (see Table 6) between the fits using lidar measured backscatter and OPC calculated backscatter, further justifies the selection of the coincident profiles. For VD, the fitting parameters between the two approaches are nearly identical.

5. Conclusions

A series of optical particle counter measurements at McMurdo from 1994 to 1999, coincident with ground-based lidar observations, has been used to obtain, for STS and NAT mixtures, an empirical relation between the particle backscatter coefficient measured by the lidar and SAD and VD calculated from the size distributions produced by the OPC. This approach has been pursued by other authors (Gobbi, 1995; Pitts et al., 2018), but starting from assumed particle size distributions.

To verify that lidar and OPC were observing the same scene, we have calculated the particle backscatter coefficients from the size distributions measured by the OPC, by using the Mie scattering theory in the approximation for spherical particles, while using appropriate refractive indices for the different PSC species, as reported in other similar studies (Hoyle et al., 2013; Pitts et al., 2018). The contribution of the NAT particles to the backscatter coefficients was then corrected by a factor 0.5 to account for the asphericity of the solid particles. Although the choice of refractive indices and the correction for the asphericity of the solid particles might be open to discussion, we showed that other, slightly different assumptions did not have a large impact on the calculated particle backscatter coefficients. Thus a subset of 15 profiles was chosen among a larger set of coincident measurements, eliminating profiles with obvious disagreements between lidar and OPC profiles.

This subset of 15 profiles, to our knowledge the largest data base used for this kind of study of polar stratospheric clouds, was then used to obtain empirical expressions of SAD and VD as a function of the particle backscatter coefficient. A least mean square fit of the form $\log(SAD) = A + B\log(\beta)$ and $\log(VD) = A + B\log(\beta)$, was performed, using the particle backscatter coefficients measured with the lidar and calculated SAD and VD from coincident OPC measurements. To compare with calculations by Pitts et al. (2018) for an ensemble of size distributions of STS particles, the lidar and OPC data have been classified as STS and NAT mixtures, ice being almost absent in these measurements. The fits performed on STS show a good agreement with the calculations by Pitts et al. (2018), within about 50%, which is nearly within the experimental uncertainty of the OPC calculations of SAD/VD which is ±40%. Additionally, there will be some uncertainty introduced by small geophysical variations in the PSCs captured by the coincident measurements which suffer from some space and time separation. An alternative approach, by fitting SAD and VD to the calculated particle backscatter coefficients, showed very similar results, but a smaller spread of the data.

Conflict of Interest

The authors declare that no competing interests are present.

Data Availability Statement

The lidar data are available at the NDACC web site ftp://ftp.cpc.ncep.noaa.gov/ndacc/station/mcmurdo/ames/lidar/. The OPC data files and size distributions are reported at the web site hosting the Wyoming in situ data http://www-das.uwyo.edu/~deshler/Data/Aer_Meas_Wy_read_me.htm and can be downloaded from ftp://cat.uwyo.edu/pub/permanent/balloon/Aerosol_InSitu_Meas/Ant_McMur.

Acknowledgments
The authors acknowledge the financial support by PNRA in the framework of the projects POAS (Particles and Ozone in the Stratosphere of Antarctica) and ACLIM (Antarctic Clouds Investigation by Multi-instrument measurements and modeling). The OPC measurements were supported by awards from the US National Science Foundation (NSF) which include OPP award numbers 9316774, 9615198, 9980594. Terry Deshler and Luca Di Liberto acknowledge a grant from the Short-Time-Mobility program of CNR, respectively in 2016 and 2009.

References

Adriani, A., Deshler, T., Di Donfrancesco, G., & Gobbi, G. (1995). Polar stratospheric clouds and volcanic aerosol during spring 1992 over McMurdo Station, Antarctica: Lidar and particle counter comparative measurements. *Journal of Geophysical Research*, *100*, 25877–25897.

Adriani, A., Deshler, T., Gobbi, G. P., Johnson, B. J., & Di Donfrancesco, G. (1992). Polar stratospheric clouds over McMurdo, Antarctica, during the 1991 spring: Lidar and particle counter measurements. *Geophysical Research Letters*, *19*, 1755–1758. https://doi.org/10.1029/92GL01941

Adriani, A., Massoli, P., Di Donfrancesco, G., Cairo, F., Moriconi, M., & Snels, M. (2004). Climatology of polar stratospheric clouds based on lidar observations from 1993 to 2001 over McMurdo Station, Antarctica. *Journal of Geophysical Research*, *109*. https://doi.org/10.1029/2004JD004800

Anthony, S. E., Onasch, T. B., Tisdale, R. T., Disselkamp, R. S., Tolbert, M. A., & Wilson, J. C. (1997). Laboratory studies of ternary H_2SO_4/HNO_3/H_2O particles: Implications for polar stratospheric cloud formation. *Journal of Geophysical Research*, *102*, 10777–10784. https://doi.org/10.1029/96JD03129

Campbell, P., & Deshler, T. (2014). Condensation nuclei measurements in the midlatitude (1982-2012) and Antarctic (1986-2010) stratosphere between 20 and 35 km. *Journal of Geophysical Research: Atmospheres*, *119*, 137–152. https://doi.org/10.1002/2013JD019710

Carslaw, K., Luo, B., & Peter, T. (1995). An analytic expression for the composition of aqueous HNO_3-H_2SO_4 stratospheric aerosols including gas-phase removal of HNO_3. *Geophysical Research Letters*, *22*, 1877–1880. https://doi.org/10.1029/95GL01668

Córdoba-Jabonero, C., Rascado, J. L., Toledo, D., Parrondo, M., Yela, M., Gil, M., & Ochoa, H. (2013). *Depolarization ratio of polar stratospheric clouds in coastal Antarctica: Comparison analysis between ground-based Micro Pulse Lidar and space-borne CALIOP observations Atmospheric Measurement Techniques* (Vol. 6, pp. 703–717). https://doi.org/10.5194/amt-6-703-2013

David, C., Bekki, S., Berdunov, N., Marchand, M., Snels, M., & Megie, G. (2005). Classification and scales of Antarctic polar stratospheric clouds using wavelet decomposition. *Journal of Atmospheric and Solar-Terrestrial Physics*, *67*, 293–300. https://doi.org/10.1016/j.jastp.2004.07.043

Deshler, T., Larsen, N., Weissner, C., Schreiner, J., Mauersberger, K., Cairo, F., et al. (2003). Large nitric acid particles at the top of an Arctic stratospheric cloud. *Journal of Geophysical Research*, *108*, 4517. https://doi.org/10.1029/2003JD003479

Deshler, T., Luo, B., Kovilakam, M., Peter, T., & Kalnajs, E. L. (2019). Retrieval of aerosol size distributions from in situ particle counter measurements: Instrument counting efficiency and comparisons with satellite measurements. *Journal of Geophysical Research: Atmospheres*, *124*, 5058–5087. https://doi.org/10.1029/2018JD029558

Deshler, T., Nardi, B., Adriani, A., Cairo, F., Hansen, G., Fierli, F., et al. (2000). Determining the index of refraction of polar stratospheric clouds above Andoya (69°N) by combining size-resolved concentration and optical scattering measurements. *Journal of Geophysical Research*, *105*, 3943–3953. https://doi.org/10.1029/1999JD900469

Di Liberto, L., Cairo, F., Fierli, F., Di Donfrancesco, G., Viterbini, M., Deshler, T., & Snels, M. (2014). Observation of polar stratospheric clouds over McMurdo (77.85°S, 166.67°E) (2006-2010). *Journal of Geophysical Research: Atmospheres*, *119*, 5528–5541. https://doi.org/10.1002/2013JD019892

Dubovik, O., Sinyuk, A., Lapyonok, T., Holben, B. N., Mishchenko, M., Yang, P., et al. (2006). Application of spheroid models to account for aerosol particle nonsphericity in remote sensing of desert dust. *Journal of Geophysical Research*, *111*, D11208. https://doi.org/10.1029/2005JD006619

Dye, J. E., Baumgardner, D., Gandrud, B. W., Kawa, S. R., Kelly, K. K., Loewenstein, M., et al. (1992). Particle size distributions in Arctic polar stratospheric clouds, growth and freezing of sulfuric acid droplets, and implications for cloud formation. *Journal of Geophysical Research*, *97*, 8015–8034. https://doi.org/10.1029/91JD02740

Engel, I., Luo, B. P., Pitts, M. C., Poole, L. R., Hoyle, C. R., Grooß, J.-U., et al. (2013). Heterogeneous formation of polar stratospheric clouds—Part 2; Nucleation of ice on synoptic scales. *Atmospheric Chemistry and Physics*, *13*, 10769–10785. https://doi.org/10.5194/acp-13-10769-2013

Erlick, C. (2006). Effective refractive indices of water and sulfate drops containing absorbing inclusions. *Journal of the Atmospheric Sciences*, *63*, 754–763. https://doi.org/10.1175/JAS3635.1

Eyring, V., Bony, S., Meehl, G. A., Senior, C. A., Stevens, B., Stouffer, R. J., & Taylor, K. E. (2016). Overview of the Coupled Model Intercomparison Project Phase 6 (CMIP6) experimental design and organization. *Geoscientific Model Development*, *9*, 1937–1958. https://doi.org/10.5194/gmd-9-1937-2016

Gobbi, G. (1995). Lidar estimation of stratospheric aerosol properties—Surface, volume, and extinction to backscatter ratio. *Journal of Geophysical Research*, *100*, 11219–11235. https://doi.org/10.1029/94JD03106

Grooß, J.-U., Engel, I., Borrmann, S., Frey, W., Günther, G., Hoyle, C. R., et al. (2014). Nitric acid trihydrate nucleation and denitrification in the Arctic stratosphere. *Atmospheric Chemistry and Physics*, *14*, 1055–1073. https://doi.org/10.5194/acp-14-1055-2014

Hamill, P., Tabazadeh, A., Kinne, S., Toon, O., & Turco, R. (1996). On the growth of ternary system HNO_3/H_2SO_4/H_2O aerosol particles in the stratosphere. *Geophysical Research Letters*, *23*, 753–756. https://doi.org/10.1029/96GL00703

Hanson, D., & Mauersberger, K. (1988). Laboratory studies of the nitric acid trihydrate: Implications for the south polar stratosphere. *Geophysical Research Letters*, *15*(8), 855–858. https://doi.org/10.1029/GL015i008p00855

Hervig, M. E., & Deshler, T. (1998). Stratospheric aerosol surface area and volume inferred from HALOE, CLAES, and ILAS measurements. *Journal of Geophysical Research*, 25345–25352.

Hervig, M. E., & Deshler, T. (2002). Evaluation of aerosol measurements from SAGE II, HALOE, and balloonborne optical particle counters. *Journal of Geophysical Research*, *107*, AAC3-1–AAC3-12. https://doi.org/10.1029/2001JD000703

Hofmann, D., & Deshler, T. (1991). Stratospheric cloud observations during formation of the Antarctic ozone hole in 1989. *Journal Geophysical Research*, *96*, 2897–2912

Hoyle, C. R., Engel, I., Luo, B. P., Pitts, M. C., Poole, L. R., Grooß, J.-U., & Peter, T. (2013). Heterogeneous formation of polar stratospheric clouds—Part 1: Nucleation of nitric acid trihydrate (NAT). *Atmospheric Chemistry and Physics*, *13*, 9577–9595. https://doi.org/10.5194/acp-13-9577-2013

Jäger, H., & Deshler, T. (2002). Lidar backscatter to extinction, mass and area conversions for stratospheric aerosols based on midlatitude balloonborne size distribution measurements. *Geophysical Research Letters*, *29*, 35-1–35-4. https://doi.org/10.1029/2002GL015609

Jäger, H., & Deshler, T. (2003). Correction to "Lidar backscatter to extinction, mass and area conversions for stratospheric aerosols based on midlatitude balloonborne size distribution measurements". *Geophysical Research Letters*, *30*, 1382. https://doi.org/10.1029/2002GL015609

Jäger, H., & Hofmann, D. (1991). Midlatitude lidar backscatter to mass, area, and extinction conversion model based on in situ aerosol measurements from 1980 to 1987. *Applied Optics*, *30*, 127–138. https://doi.org/10.1364/AO.30.000127

Koop, T., Biermann, U., Raber, W., Luo, B., Crutzen, P., & Peter, T. (1995). Do stratospheric droplets freeze above the ice frost point? *Geophysical Research Letters*, *22*, 917–920. https://doi.org/10.1029/95GL00814

Kovilakam, M., & Deshler, T. (2015). On the accuracy of stratospheric aerosol extinction derived from in situ size distribution measurements and surface area density derived from remote SAGE II and HALOE extinction measurements. *Journal of Geophysical Research: Atmospheres*, *120*, 8426–8447. https://doi.org/10.1002/2015JD023303

Kremser, S., Thomason, L. W., von Hobe, M., Hermann, M., Deshler, T., Timmreck, C., et al. (2016). Stratospheric aerosol—Observations, processes, and impact on climate. *Reviews of Geophysics*, *54*, 278–335. https://doi.org/10.1002/2015RG000511

Liu, L., Mishchenko, M. I., Cairns, B., Carlson, B. E., & Travis, L. D. (2006). Modeling single-scattering properties of small cirrus particles by use of a size-shape distribution of ice spheroids and cylinders. *Journal of Quantitative Spectroscopy and Radiative Transfer*, *101*, 488–497. https://doi.org/10.1016/j.jqsrt.2006.02.040

Lowe, D., & MacKenzie, A. R. (2008). Polar stratospheric cloud microphysics and chemistry. *Journal of Atmospheric and Solar-Terrestrial Physics*, *70*, 13–40. https://doi.org/10.1016/j.jastp.2007.09.011

Luo, B., Krieger, U. K., & Peter, T. (1996). Densities and refractive indices of $H_2SO_4/HNO_3/H_2O$ solutions to stratospheric temperatures. *Geophysical Research Letters*, *23*, 3707–3710. https://doi.org/10.1029/96GL03581

Luo, B. P., Voigt, C., Fueglistaler, S., & Peter, T. (2003). Extreme NAT supersaturations in mountain wave ice PSCs: A clue to NAT formation. *Journal of Geophysical Research*, *108*, 4441. https://doi.org/10.1029/2002JD003104

Mehrtens, H., von Zahn, U., Fierli, F., Nardi, B., & Deshler, T. (1999). Type I PSC-particle properties: Measurements at ALOMAR 1995 to 1997. *Geophysical Research Letters*, *26*, 603–606. https://doi.org/10.1029/1999GL900027

Mercer, J. L., Kröger, C., Nardi, B., Johnson, B., Chipperfield, M., Wood, S. W., et al. (2007). Comparison of measured and modeled ozone above McMurdo Station, Antarctica, 1989–2003, during austral winter/spring. *Journal of Geophysical Research*, *112*, D19307. https://doi.org/10.1029/2006JD007982

Middlebrook, A. M., Berland, B. S., George, S. M., Tolbert, M. A., & Toon, O. B. (1994). Real refractive indices of infrared-characterized nitric-acid/ice films: Implications for optical measurements of polar stratospheric clouds. *Journal of Geophysical Research*, *99*, 25655–25666. https://doi.org/10.1029/94JD02391

Mishchenko, M. I., Travis, L. D., Kahn, R. A., & West, R. A. (1997). Modeling phase functions for dustlike tropospheric aerosols using a shape mixture of randomly oriented polydisperse spheroids. *Journal of Geophysical Research*, *102*, 16831–16847. https://doi.org/10.1029/96JD02110

Mishchenko, M. I., Travis, L. D., & Mackowski, D. W. (1996). T-matrix computations of light scattering by nonspherical particles: A review. *Journal of Quantitative Spectroscopy and Radiative Transfer*, *55*, 535–575. https://doi.org/10.1016/0022-4073(96)00002-7

Morgenstern, O., Giorgetta, M. A., Shibata, K., Eyring, V., Waugh, D. W., Shepherd, T. G., et al. (2010). Review of the formulation of present-generation stratospheric chemistry-climate models and associated external forcings. *Journal of Geophysical Research*, *115*, d00M02. https://doi.org/10.1029/2009JD013728

Morgenstern, O., Hegglin, M. I., Rozanov, E., O'Connor, F. M., Abraham, N. L., Akiyoshi, H., et al. (2017). Review of the global models used within phase 1 of the Chemistry–Climate Model Initiative (CCMI). *Geoscientific Model Development*, *10*, 639–671. https://doi.org/10.5194/gmd-10-639-2017

Peter, T. (1997). Microphysics and heterogeneous chemistry of polar stratospheric clouds. *Annual Review of Physical Chemistry*, *48*, 785–822.pMID: 15012456. https://doi.org/10.1146/annurev.physchem.48.1.785

Pitts, M. C., Poole, L. R., & Gonzalez, R. (2018). Polar stratospheric cloud climatology based on CALIPSO spaceborne lidar measurements from 2006–2017. *Atmospheric Chemistry and Physics*, *18*, 10881–10913. https://doi.org/10.5194/acp-18-10881-2018

Prata, A. T., Young, S. A., Siems, S. T., & Manton, M. J. (2017). Lidar ratios of stratospheric volcanic ash and sulfate aerosols retrieved from CALIOP measurements. *Atmospheric Chemistry and Physics*, *17*, 8599–8618. https://doi.org/10.5194/acp-17-8599-2017

Ridley, D. A., Solomon, S., Barnes, J. E., Burlakov, V. D., Deshler, T., Dolgii, S. I., et al. (2014). Total volcanic stratospheric aerosol optical depths and implications for global climate change. *Geophysical Research Letters*, *41*, 7763–7769. https://doi.org/10.1002/2014GL061541

Rosen, J. M. (1964). The vertical distribution of dust to 30 kilometers. *Journal fo Geophysical Research*, *69*, 4673–4676.

Rosen, J. M., Hofmann, D. J., & Kaselau, K. H. (1978). Vertical profiles of condensation nuclei. *Journal of Applied Meteorology*, *17*, 1737–1740. https://doi.org/10.1175/1520-0450(1978)017⟨1737:VPOCN⟩2.0.CO;2

Scarchilli, C., Adriani, A., Cairo, F., Di Donfrancesco, G., Buontempo, C., Snels, M., et al. (2005). Determination of polar stratospheric cloud particle refractive indices by use of in situ optical measurements and T-matrix calculations. *Applied Optics*, *44*, 3302–3311.

Snels, M., Cairo, F., Colao, F., & Di Donfrancesco, G. (2009). Calibration method for depolarization lidar measurements. *International Journal of Remote Sensing*, *30*, 5725–5736. https://doi.org/10.1080/01431160902729572

Snels, M., Colao, F., Cairo, F., Shuli, I., Scoccione, A., De Muro, M., et al. (2021). Quasi-coincident observations of polar stratospheric clouds by ground-based lidar and CALIOP at Concordia (Dome C, Antarctica) from 2014 to 2018. *Atmospheric Chemistry and Physics*, *21*(3), 2165–2178. https://dx.doi.org/10.5194/acp-21-2165-2021

Snels, M., Colao, F., Shuli, I., Scoccione, A., De Muro, M., Pitts, M., et al. (2020). Quasi-coincident observations of polar stratospheric clouds by ground-based lidar and CALIOP at Concordia (Dome C, Antarctica) from 2014 to 2018. *Atmospheric Chemistry and Physics Discussions*, 1–22. https://doi.org/10.5194/acp-2020-972. Retrieved from https://acp.copernicus.org/preprints/acp-2020-972/

Snels, M., Scoccione, A., Di Liberto, L., Colao, F., Pitts, M., Poole, L., et al. (2019). Comparison of Antarctic polar stratospheric cloud observations by ground-based and spaceborne lidars and relevance for chemistry-climate models. *Atmospheric Chemistry and Physics*, 955–972. https://doi.org/10.5194/acp-19-955-2019

Solomon, S. (1999). Stratospheric ozone depletion: A review of concepts and history. *Reviews of Geophysics*, *37*, 275–316. https://doi.org/10.1029/1999RG900008. Retrieved from https://agupubs.onlinelibrary.wiley.com/doi/abs/10.1029/1999RG900008

Steele, H. M., & Hamill, P. (1981). Effects of temperature and humidity on the growth and optical properties of sulphuric acid—water droplets in the stratosphere. *Journal of Aerosol Science*, *12*, 517–528. https://doi.org/10.1016/0021-8502(81)90054-9

Tabazadeh, A., Djikaev, Y. S., Hamill, P., & Reiss, H. (2002). Laboratory evidence for surface nucleation of solid polar stratospheric cloud particles. *The Journal of Physical Chemistry A*, *106*, 10 238–10 246. https://doi.org/10.1021/jp021045k

Thomason, L., & Peter, T. (2006). *SPARC assessment of stratospheric aerosol properties (ASAP)* (Tech. Rep.): SPARC report, 4(322). SPARC. Retrieved from http://www.sparc-climate.org/publications/sparc-reports/

Thomason, L. W., Ernest, N., Millán, L., Rieger, L., Bourassa, A., Vernier, J.-P., et al. (2018). A global space-based stratospheric aerosol climatology: 1979–2016. *Earth System Science Data*, *10*, 469–492. https://doi.org/10.5194/essd-10-469-2018

Voigt, C., Schlager, H., Luo, B. P., Dörnbrack, A., Roiger, A., Stock, P., et al. (2005). Nitric Acid Trihydrate (NAT) formation at low NAT supersaturation in Polar Stratospheric Clouds (PSCs). *Atmospheric Chemistry and Physics*, *5*, 1371–1380. https://doi.org/10.5194/acp-5-1371-2005

Ward, S. M., Deshler, T., & Hertzog, A. (2014). Quasi-Lagrangian measurements of nitric acid trihydrate formation over Antarctica. *Journal of Geophysical Research: Atmospheres*, *119*, 245–258. https://doi.org/10.1002/2013JD020326

Warren, S. G., & Brandt, R. E. (2008). Optical constants of ice from the ultraviolet to the microwave: A revised compilation. *Journal of Geophysical Research*, *113*, d14220. https://doi.org/10.1029/2007JD009744

Weiss, F., Kubel, F., Gálvez, O., Hoelzel, M., Parker, S. F., Baloh, P., et al. (2016). Metastable nitric acid trihydrate in ice clouds. *Angewandte Chemie*, *55*, 3276–3280. https://doi.org/10.1002/anie.201510841

Zhu, Y., Toon, O. B., Kinnison, D., Harvey, V. L., Mills, M. J., Bardeen, C. G., et al. (2018). Stratospheric aerosols, polar stratospheric clouds, and polar ozone depletion after the Mount Calbuco eruption in 2015. *Journal of Geophysical Research: Atmospheres*, *123*, 12308–12331. https://doi.org/10.1029/2018JD028974. Retrieved from https://agupubs.onlinelibrary.wiley.com/doi/abs/10.1029/2018JD028974